Results in Engineering 21 (2024) 101770

Contents lists available at ScienceDirect

Results in Engineering

journal homepage: www.sciencedirect.com/journal/results-in-engineering

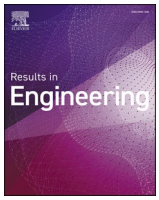

Statistical analysis of modelling approaches for CFD simulations of high-pressure natural gas releases

Fabio Ferrario [a,b], Valentina Busini [a,*]

[a] Department of Chemistry, Materials and Chemical Engineering "Giulio Natta", Politecnico di Milano, 20131, Milan, Italy
[b] Joint Research Centre, European Commission, Petten, the Netherlands

ARTICLE INFO

Keywords:
Natural gas
High-pressure release
Computational fluid dynamics
Equivalent diameter
Pipeline rupture

ABSTRACT

The use of computational fluid dynamics (CFD) in process safety to estimate the risk of a given incidental scenario has become ever more present in common industry practice. The simulation of high-pressure, compressible natural gas jets is often performed by modelling its source with a simpler notional diameter approach, such that the highly computationally expensive nearfield zone need not to be simulated; this is particularly determining when simulating a gas release in complex scenario like liquid natural gas (LNG) regasification plants. In this study, we analysed the structure of compressible and incompressible jets, using Birch 1984 (B84) and Birch 1987 (B87) models. In this work, a study on the positioning of the notional diameter with respect to the real orifice of the released gas is performed, along with a statistical analysis to assess the limits of the simpler model approaches.

It was found that no spacing is needed between the virtual and real sources, as the potential core generated by the simpler model is as large as the fully simulated nearfield zone by the compressible model. Additionally, an end-of-transition zone position correlation is reported. The incompressible models can be used instead of the fully compressible model for a wide range of release conditions, with both models providing accurate predictions of axisymmetrical mole fraction, temperature, and velocity profiles between 2.5 and 130 bar of storage pressure at a 1-inch orifice diameter. However, as the diameter increases, B84 is not a viable model for a "full bore" (10-inch diameter size) release at 65 bar. While B84 is reliable, B87 is the superior model for its ability to account for the compressible effects of the expansion. Therefore, B87 should be used when simulating cases where temperature is of particular interest to the user.

1. Introduction

The process of storage and handling of natural gas can take many forms in the energy industry, ranging from its complete liquefaction into Liquid Natural Gas (LNG, resulting from compression and cooling) used in LNG carriers, to high energy density pressurized natural gas used in the natural gas distribution network (through compression stations) [1]. With pipelines that have operating pressures that can range from 10 to 100 bar [2], the release of the pressurized gas leads to the formation of compressible jets that can reach axial extensions of multiple meters when fully developed [3].

Natural gas is a non-toxic, flammable gas that, if present in excessive quantities in the environment, can still be dangerous to humans as it can displace oxygen-filled air from the lungs, acting as an asphyxiant [4]. Furthermore, when an accidental release scenario in an industrial setting develops, the dilution of the jet will allow the gas-air mixture to reach methane (the main component of natural gas) concentration values that are within its flammability range, substantially increasing the risk of flash fires and jet fires [3]. A throughout risk assessment that considers the area of effect will be necessary to protect workers, the environment, and equipment when prevention is not possible.

A compressible jet can be fragmented into the following zones, where different phenomena due to the adiabatic expansion of the gas, tend to occur [5]:

- Nearfield zone
- Transitional zone
- Farfield zone

The pressure, temperature, and velocity of the nearfield zone change rapidly within a few centimetres of distance from the source as a

* Corresponding author.
E-mail address: valentina.busini@polimi.it (V. Busini).

https://doi.org/10.1016/j.rineng.2024.101770
Received 13 September 2023; Received in revised form 12 December 2023; Accepted 7 January 2024
Available online 10 January 2024

Nomenclature

C_d	Discharge Coefficient [−]
C_p	Specific heat capacity [J/mol K]
d	Real orifice diameter [m]
d_{ps}	Equivalent diameter [m]
g	Gravitational acceleration [9.81 m/s]
P	Pressure [Pa]
R	Ideal gas constant [8.314 J/mol K]
T	Temperature [K]
v	Velocity [m/s]
Y_i	Predicted data point [−]
$\overline{Y}$	Mean value of experimental data [−]
$\widehat{Y}_I$	Experimental data point [−]
X_{Mach}	Distance from the source to the Mach disk [m]
X_{ETZ}	Distance from the source to the end of the transition zone [m]

Subscripts

i,j	Indices
1,2,3	Levels
Amb	Parameter in Ambient condition
bulk	Parameter in Bulk condition

Greek symbols

γ	Isentropic coefficient [−]
ρ	Density [kg/m^3]
μ	Dynamic Viscosity [Pa s]

Abbreviations

B84	Birch 1984
B87	Birch 1987
BOI	Body of influence
CFD	Computational fluid dynamics
FVM	Finite Volume Method
GM	Geometric Mean Bias
GV	Geometric Variance
GUI	Graphical User Interface
RANS	Reynolds-Averaged Navier-Stokes
SST	Shear Stress Transport
LNG	Liquid natural gas
LFL	Lower Flammability Limit
MW	Molar Weight

consequence of substantial expansion of the fluid. In the transition zone, effects from pressure variation are minor, and longitudinal and radial variations of the temperature and velocity profile are less pronounced until the pressure in the jet equalizes with the surrounding pressure. Lastly, the farfield zone is the section of the jet where it is fully expanded, with longitudinal velocity and temperature are proportional to the distance from the source and its dissipation is mostly dominated by internal buoyancy and ambient turbulence forces [2].

While release conditions can have a strong effect on the structure of a jet, the geometry of the environment in which the gas expands can substantially affect the extension of the cloud and its dissipation as air dilutes the gas. To consider the maximum area of impact if ignition occurs, the maximum extension of the cloud is measured at the lower concentration limit where a methane-air mixture is flammable at standard conditions, the Lower Flammability Limit (LFL) of methane in the air [3].

To accomplish the risk analysis, a multitude of prediction models can be employed. Most commonly, the use of integral dispersion models is a popular option for the resolution of the problem, due to it being relatively easy and quick to employ. A major limit to the integral models is their inability to account for interactions between the expanding jet and surrounding obstacles, which limits the cases that can be explored to only free jet simulations (*i.e.*, expanding jets that do not interact with any obstacles, not even the ground) [6].

More complex models must be used for cases where a jet-obstacle interaction is expected. Computational Fluid Dynamics (CFD) is a powerful approach to modelling fluid dynamic problems, where the Finite Volume Method (FVM) is used to discretize a volume (called domain) into sub-volumes (called cells) that solve a set of conservation equations to simulate the desired fluid dynamic phenomenon [7].

The numerical method has shown itself to be highly reliable in fields of work that are beyond the scope of high-pressure fluid safety. Hasan et al. [8] showed how the method can be utilized for the design of an exhaust gas recirculation system to reduce the temperature and oxygen level in internal combustion vehicles. It allowed for the comparison of various static vortex generators in a single and array configuration. Beyond its predictive capabilities, is also able to simulate the functionality of existing facilities, like Hossain et al. [9] demonstrated in their work on currently used coal combustion facilities in typical power plants in Bangladesh. The model then was used to test the implementation of carbon capture and sequestration technology to assess its feasibility in already existing facilities.

It is thus suggested that, for a vast majority of cases of high-pressure natural gas releases, a numerical simulation should be performed. The question of what CFD-codes to employ can be somewhat tantalising, as the choice between open source software (*e.g.,* OpenFoam [10]) and commercial software (*e.g.,* Fluent [11]), is very much dependent on the specific necessities of the user. A throughout comparison between open-source codes, OpenFOAM and MFiX, was done by Reyes-Urritia et al. [12] for a bubbling fluidised bed system. The study highlighted the limitations of both software, relating that both can replicate experimental data accurately, with low versatility on the meshing step of the process for MiFX. The choice of this study to use a commercial code was related to a more user-friendly GUI and modular approach that Ansys Workbench incentivises on their software. Furthermore, the Ansys Suite provides a powerful tool in Ansys meshing that permits the use of a meshing technique not readily available in OpenFOAM, Body of Influence (which will be explored further in section 2.3.1), which was validated by authors performing similar work [13–15] to the one explored in this paper.

Proper simulation of the expansion phenomenon of the jet can be done with a high number of cells to rendition the large pressure, temperature and velocity gradients that are expected in a compressible, under-expanded jet, leading to longer simulation times.

To expedite the simulation process and computational demand, a multitude of simplified models can be applied to simulate the same compressible under-expanded jet as an incompressible expanded jet, through the incompressible model. This method consists of the simplification of the compressible jet by assuming a stable nearfield zone, as well as the conservation of mass [16,17], and later on momentum [18,19] within the jet. As explained in later sections, this permits the sidestepping of the simulation of the highly expensive nearfield zone, allowing a non-expanding jet to be simulated with high reliability with experimental data. This strategy was successfully implemented by Cui et al. [20] to quantify the effect of the accidental release of a high pressure hydrogen jet in a hydrogen refuelling station, where different leakage angles were tested and compared. The study allowed for a quantitative and qualitative analysis of the effect of wind direction and speed on the hydrogen cloud, along with the morphology of the structure of the refuelling station. Several studies that identified the effect of

natural gas cloud interactions with differing geometries were carried out by Colombini et al. [13–15,21,22], who reported great insights into the fluid dynamic interactions between the natural gas jet and complicated obstacles that will affect the area of effect of the gas cloud.

There is a wide range of incompressible models present in literature that make differing assumptions to achieve comparable results. Models by Birch in 1984 [16] and 1987 [18], Ewan & Moodie [17] and Schefer [19] were all compared by Papanikolaou et al. [23] to assess their reliability against experimental data of hydrogen high-pressure gas release. It was found that in order of performance, Birch1987 and Schefer generally performed better, followed by Birch1984 and, lastly, Ewan. In terms of the turbulence model, the k-ω Shear Stress Transport (k-ω SST) [24] was the most well-performing. Further studies on the reliability of the incompressible model were carried out by Forsell [25], where a fully simulated compressible methane jet was compared to various simplified models. The assumption of no air entrainment by the equivalent diameter approaches tends to lead to an over-prediction of the size of the cloud.

Considering the limitations of the incompressible model, an immediate question arises on how the compressible and incompressible jets differ. No direct effort to test the range of viability of the incompressible model has been found in the literature. The question this paper aims to answer is to what degree can the no-compressibility condition applied for equivalent diameter models be acceptable and when these models start to fail due to simulation instabilities and inaccuracies.

Thus, a variety of release conditions of storage pressure and orifice diameter of the source are simulated. The compressible (which simulates the nearfield zone) model and only two of the incompressible models are used:

- Birch 1984, which is the best performing one, of the mass conservation assumptions, in the tests by Papanikolaou [23].
- Birch 1987, which is the best performing one, of the momentum and mass conservation assumptions, in the tests by Papanikolaou [23].

An analysis of the structure of the jet is performed. It is stated within the literature that the positioning of the virtual source used in the incompressible approach is the same as the Mach disk generated by the compressible jet [26]. In this paper, it is demonstrated that this is not the case. Furthermore, as an extension to the analysis of the structure of the jet, an empirical correlation for the definition of the ending of the transition zone (*i.e.,* the beginning of the farfield zone) is reported. The release conditions considered were chosen to quantify, through a statistical analysis of the mole fraction, temperature, and velocity profile along the jet axis, the limits of the incompressible models. Lastly, it is then defined when it is ideal to use one approach rather than the other.

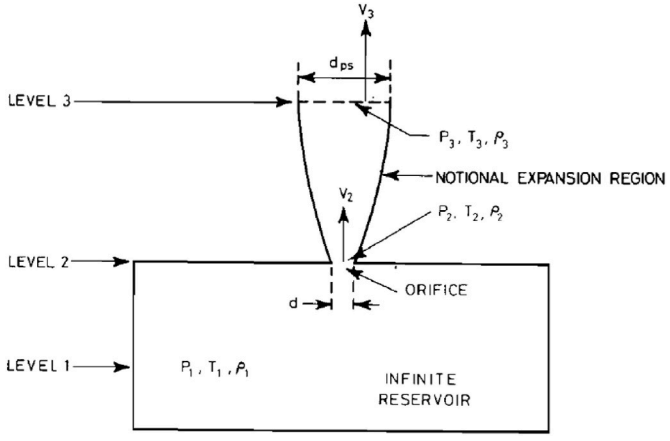

Fig. 1. Schematic of the three level model from Birch et al. [7].

2. Material and methods

In the following section, the numerical method is discussed, along with the core differences between modelling a compressible and incompressible jet. A baseline case is presented to explain the simulation methodology for all subsequent cases.

2.1. Governing equations of the computational method

The software used to run the CFD simulations was Ansys® Workbench 2019R3, while the post-processing was performed with MATLAB® R2022a. The CFD method relies on the simulation of physical phenomena by solving a system of linear conservation equations, defined as Reynolds-Averaged Navier-Stokes (RANS) equations. These are balance equations of mass, momentum, and energy. They are the following [11]:

Continuity Equation:

$$\frac{\partial \rho}{\partial t}+\frac{\partial}{\partial x_i}(\rho u_i)=0 \tag{1}$$

Momentum Equation:

$$\frac{\partial}{\partial t}(\rho u_i)+\frac{\partial}{\partial x_j}\left(\rho u_i u_j\right)=-\frac{\partial p}{\partial x_i}+\frac{\partial}{\partial x_j}\left[\mu\left(\frac{\partial u_i}{\partial x_j}+\frac{\partial u_j}{\partial x_i}-\frac{2}{3}\delta_{ij}\frac{\partial u_j}{\partial x_i}\right)\right]+\frac{\partial}{\partial x_j}\left(-\rho\overline{u_i' u_j'}\right)+\rho g_i \tag{2}$$

where i and j are direction vectors for the parameters, while u_i and u_j are velocity components. δ_{ij} is a unit tensor that is equals to 1 when $i=j$, and equals to 0 when $i\neq j$. u_i' and u_j' are fluctuating velocity components, which are defined as Reynolds Stresses when displayed as $-\rho\overline{u_i' u_j'}$..

Energy Equation:

$$\frac{\partial(\rho E)}{\partial t}+\nabla\cdot\left(\vec{v}(\rho E+p)\right)=\nabla\cdot\left(k_{eff}\nabla T-\sum_j h_j\vec{J}_j+\vec{v}\left(\bar{\bar{\tau}}_{eff}\cdot\vec{v}\right)\right) \tag{3}$$

where E is total energy, $\vec{J}_j$ is the diffusion flux of species j, $\vec{v}$ is the velocity vector field, k_{eff} is effective conductivity and $\bar{\bar{\tau}}_{eff}$ is the effective fluid stress tensor.

As mentioned in the previous section, Papanikolaou [23] demonstrated that the best closure model to represent turbulent effects when simulating the release of high-pressure jets is the k-ω SST. Thus, every simulated jet relied on the aforementioned closure method.

2.2. High-pressure jets: compressible and incompressible approaches

In the context of risk analysis, the main focus for the assessment is in the farfield of the jet, as the maximum extent of natural gas, as LFL concentrations, manifests when the jet is fully expanded. However, it is of paramount importance to avoid errors in the source term determination because it could cause errors in the farfield prediction.

To adequately quantify the reliability of the incompressible approaches, a comparison between a simulation that accurately models the nearfield zone of the jet and ones that use the proposed Birch approaches is necessary.

2.2.1. Compressible approach

By assuming an infinite reservoir with a fixed storage pressure and temperature, that does not change as the flow exits, the orifice conditions can be defined by way of an isentropic expansion. Thus, the following equations can be used to calculate the exit pressure, exit temperature, and exit velocity at the orifice to set the compressible simulations [27]:

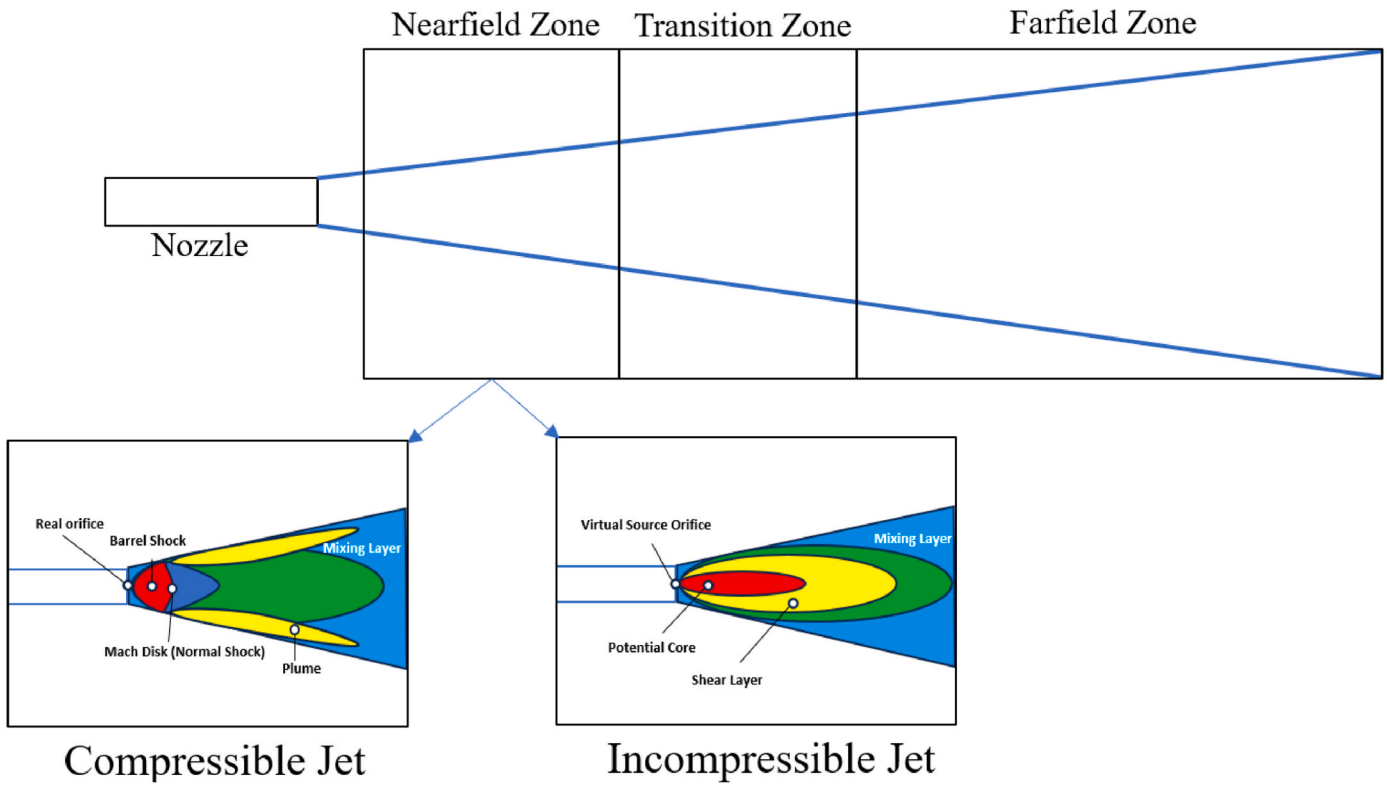

Fig. 2. High pressure jet schematic for compressible and incompressible jets. The incompressible jet simulation greatly simplifies the structure of the nearfield zone.

$$P_2 = P_1\left(\frac{2}{\gamma+1}\right)^{\frac{\gamma}{\gamma-1}} \tag{4}$$

$$T_2 = T_1\left(\frac{2}{\gamma+1}\right) \tag{5}$$

$$v_2 = \sqrt{\frac{RT_2\gamma}{MW}} \tag{6}$$

where P_1 and T_1 are pressure and temperature at storage conditions (velocity v_1 in the storage is considered negligible) in level 1, while P_2, T_2, and v_2 are pressure, temperature, and velocity at orifice conditions in level 2, as shown in Fig. 1. The value γ is the isentropic coefficient and MW is the molar weight of the released gas (methane in this work), while R is the ideal gases constant.

As demonstrated in Ref. [28], these values are enough to simulate a compressible jet through the CFD approach.

2.2.2. Birch 1984 approach

Birch's 1984 (B84) approach considers the hypothesis of mass conservation in the space between the orifice of the real source (Level 2) and the surface of the virtual source with the equivalent diameter, d_{ps}, at level 3, as shown in Fig. 1, so that the flowrate calculated at the orifice is the same as the one defined at the virtual surface.

By nature of the approach, the pressure at the virtual source will be the same as the surrounding environment. It also assumed that entrainment of air heats up the jet enough to consider its temperature equals to bulk temperature. By considering that the exit velocity of the jet from the virtual source is equivalent to sonic velocity, its parameters are the following [16]:

$$P_3 = P_{amb} \tag{7}$$

$$T_3 = T_{bulk} \tag{8}$$

$$v_3 = \sqrt{\frac{RT_3\gamma}{MW}} \tag{9}$$

$$d_{ps} = d\sqrt{C_d\left(\frac{P_1}{P_{amb}}\right)\left(\frac{T_3}{T_1}\right)^{\frac{1}{2}}\left(\frac{2}{\gamma+1}\right)^{\frac{(\gamma+1)}{2(\gamma-1)}}} \tag{10}$$

where P_3, T_3 and v_3 are pressure, temperature and exit velocity of the virtual source where the diameter equals to the equivalent diameter d_{ps}, as shown on Level 3 in Fig. 1. C_d is the discharge coefficient, and d is the diameter of the real orifice.

2.2.3. Birch 1987 approach

Birch's 1987 (B87) approach is an updated version of the 1984, which defines another equivalent diameter by invoking the conservation of mass and momentum through the expansion zone between the real orifice and the surface virtual source. While the pressure at the virtual source is still the ambient pressure, the temperature is estimated to be roughly equal to the storage temperature due to the rapid warm up of the jet post shock region. The set of equations of the previous section are updated as follows [18]:

$$P_3 = P_{amb} \tag{11}$$

$$T_3 = T_1 \tag{12}$$

$$v_3 = v_2 C_d + \left(\frac{P_2 - P_{amb}}{\rho_2 v_2 C_d}\right) \tag{13}$$

$$d_{ps} = d\sqrt{C_d\left(\frac{P_1}{P_{amb}}\right)\left(\frac{v_2}{v_3}\right)\left(\frac{2}{\gamma+1}\right)^{\frac{1}{(\gamma-1)}}} \tag{14}$$

where P_3, T_3 and v_3 are pressure, temperature and exit velocity of the virtual source with diameter equals to the equivalent diameter d_{ps}, as shown on Level 3 in Fig. 1. ρ_2 is the gas density at the real orifice and v_2

Table 1
Thermophysical parameters of natural gas used by Birch et al. [16].

Molar Weight [g/mol]	C_p (288 K) [J/K mol]	γ [−]
17.34	1850	1.35

Table 2
Inlet properties for each model for the base scenario.

	Compressible	B84	B87
Inlet Diameter [mm]	25.4	145.82	114.38
Mass Flowrate [kg/s]	5.18	5.18	5.18

is the sound velocity at the orifice condition (equation (3)).

2.3. Model setup: base case scenario and simulation parameters

The base case scenario is used to exemplify the basic setup for a compressible simulation and an incompressible simulation using Birch's approaches. This case is based on a previous work [13] that involves a realistic situation of industrial interest with an accidental release of a horizontally oriented high pressure natural gas jet adjacent to the ground. The considered case has a storage absolute pressure of 65 bar, storage temperature of 278.15 K, and a bulk temperature of 300 K, with a real orifice diameter of 0.0254 m (1 inch). The released height was chosen so that the developing jet did not interact with the ground at a molar fraction equal to the LFL value of 5% for natural gas, and the discharge coefficient C_d was set to 0.85.

Each model referenced is listed below, which generate the jets exemplified in Fig. 2:

- The compressible model uses the real orifice diameter as inlet and orifice conditions from section 2.2.1
- The incompressible model of B84 uses its equivalent diameter as inlet dimension and virtual source conditions from section 2.2.2
- The incompressible model of B87 uses its equivalent diameter as inlet dimension and virtual source conditions from section 2.2.3

Natural gas parameters are listed in Table 1, where the molar weight is a weighted average value of all natural gas components (with a methane content between 92 and 92.4% [16]). Furthermore, the inlet diameter and mass flow rate of each model are listed in Table 2.

Since the base case is an outdoor incidental release, the worst case is having the wind blow along the axis of the jet, elongating the dispersion phase of the jet to further distances. A velocity profile is defined for the air inlet behind the release inlet, which is estimated by the following logarithmic equation:

$$v = v_{10}\frac{log\left(\frac{y}{y_0}\right)}{log\left(\frac{y_{10}}{y_0}\right)} \tag{15}$$

where $v_{10} = 5\,m/s$ is the reference velocity at $y_{10} = 10$ m from the ground. The value y_0 is the height at which the wind velocity parallel to the ground is equals to zero. Thus, y_0 is 1/10 of the ground roughness height of the simulated ground surface. Concrete has a roughness height of 0.01, making $y_0 = 0.001$.

2.3.1. Geometry and mesh for the base scenario

The geometry of the domain was based on previous works [13–15, 21,22,29,30] which were performed by using the B84 model. Fig. 3 displays a schematic of the domain and the nomenclature of its parameters.

These domain parameters have been proven to be effective with an extensive number of simulation scenarios, and are as follows:

- W is the width of the domain at 32.2 m;
- H is the height of the domain at 35 m;
- L is the length of the domain at 105 m;
- L_u is the nozzle length at 7 m;
- Inlet diameter is listed in Table 2.

The dimensional parameters of the domain are extensively larger than the maximum extension reached by a methane cloud diluted to an LFL concentration. The bigger the calculation volume for the domain, the less affected will the jet be by pressure gradients along the boundaries as it fully expands.

Because of the size of the domain, an adaptive tetrahedral mesh design was applied, where Body of Influence (BOI) lines are used to selectively discretize the volume. A high number of cells near the nozzle are modelled, with the number decreasing as the distance from the nozzle increases. Each model will have different prerequisites, as shown

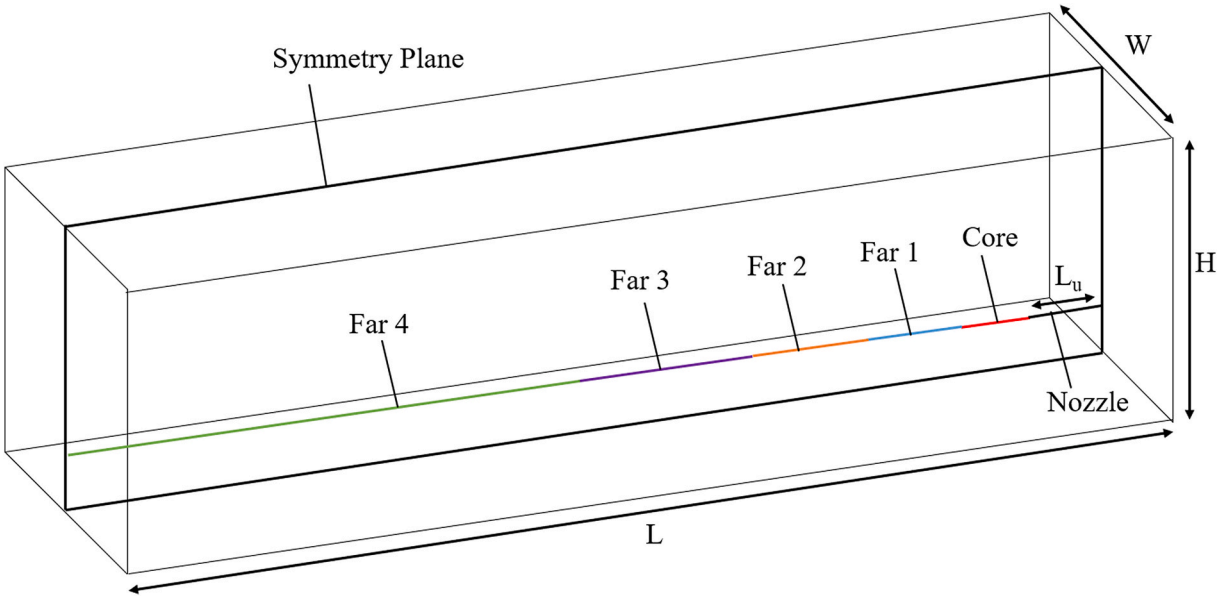

Fig. 3. Geometry of the domain, with Body of Influence lines and symmetry plane.

Table 3
Geometrical and mesh characteristics of the BOI lines.

	Core	Far 1	Far 2	Far 3	Far 4
BOI size [m]	6	8	8	10	66
Inlet Diameter ***[m]***	10	7	5	1.7	0.8
Cell Size ***[m]***	Growth Rate : 1.075	Growth Rate : 1.1	Growth Rate : 1.15	Growth Rate : 1.175	Growth Rate : 1.2

Table 4
Boundary Layer characteristics for the base scenario.

Boundary Layers	Boundary Type	Compressible	B84	B87
Air Inlet	Velocity Inlet	V_z = Velocity profile T = 300 K	V_z = Velocity profile T = 300 K	V_z = Velocity profile T = 300 K
Left Side	Velocity Inlet	V_z = Velocity profile T = 300 K	V_z = Velocity profile T = 300 K	V_z = Velocity profile T = 300 K
Sky	Velocity Inlet	V_z = 5.68 m/s T = 300 K	V_z = 5.68 m/s T = 300 K	V_z = 5.68 m/s T = 300 K
Outlet	Pressure Outlet	Gauge Pressure = 0 Pa T = 300 K	Gauge Pressure = 0 Pa T = 300 K	Gauge Pressure = 0 Pa T = 300 K
Methane Inlet	Mass Inlet	Refer to Table 2 Initial Pressure Gauge = 3,388,207 Pa T total = 271.32 K	Refer to Table 2 – T static = 300 K	Refer to Table 2 – T static = 278.15 K
Nozzle	Wall	Roughness height = 0 m	Roughness height = 0 m	Roughness height = 0 m
Ground	Wall	Roughness height = 0.01 m	Roughness height = 0.01 m	Roughness height = 0.01 m

in Table 3.

Mesh parameters of the methane gas inlet and nozzle wall are equals to the core and Far 2 BOI cell size respectively. It is important to note that cell size will vary since the inlet diameter will vary depending on the model used for the simulation, as seen in Table 2.

The inlet diameter referenced in Table 2 uses the real orifice diameter for the compressible model and the equivalent diameter for incompressible models. As stated in the Fluent theory manual [11], a rule of thumb for the minimum number of cells needed to cover a boundary layer accurately, is 10 cells. Subsequentially, the cell size of the methane inlet boundary was modified to accommodate this rule, starting from the values employed by Romano et al. [29].

To reduce the computational load, a symmetry plane methodology was used to symmetrically cut the domain in half, halving the number of cells. For the most computationally complex cases, the resulting number of cells is 8×10^6 for the compressible model, 1.4×10^6 for the incompressible B84 model and 2.65×10^6 for the incompressible B87 model.

2.3.2. Mesh independence

To prevent results from being dependent on the number of cells simulated, a mesh independence test was performed by doubling the diameter-to-cell size ratio indicated in Table 3 for each model used for the base scenario. By comparing the mole fraction profile between the cases with the denser mesh and the cases with the mesh created by using parameters from Table 3, a difference of less than 1% was found between them. Due to the stated result, cases that use Table 3 parameters to mesh the domain can be considered mesh independent.

2.3.3. Fluent setup for the base scenario

Each boundary layer was named as they must be defined in the Fluent module, along with solver turbulence models. To use multiple species of air and natural gas, the multispecies model was used as a mixture species. As referenced in section 2.1, the turbulent closure model of Shear Stress Transport (SST) was employed for all suggested jet models [11].

In Table 4 all boundary characteristics are listed.

Velocities for directions along the x-axis and y-axes for velocity inlet boundaries are set as -1×10^{-9} m/s to avoid domain boundary effects that could interfere with the jet being simulated. The compressible model must use the ideal gas law model to simulate the nearfield zone. Inversely, the incompressible model uses the incompressible ideal gas law that greatly simplifies and speeds up simulation time.

Table 5
Cases performed for each model, storage temperature of 278.15 K and ambient temperature of 300 K.

Compressible Model					
Storage pressure [bar]	Orifice diameter [m]	Initial pressure Gauge [Pa]	Total Temperature T_2 [K]	Mass flowrate [kg/s]	Speed of sound v_2 [m/s]
2.5	0.0254	32,880	271.32	0.1993	440.78
32.5	0.0254	1,643,440	271.32	2.5915	440.78
65	0.0127	3,388,207	271.32	1.2957	440.78
65	0.0381	3,388,207	271.32	11.662	440.78
65	0.0508	3,388,207	271.32	20.732	440.78
65	0.1016	3,388,207	271.32	82.93	440.78
65	0.2540	3,388,207	271.32	518.32	440.78
100	0.0254	5,267,180	271.32	7.974	440.78
100	0.1158	5,267,180	271.32	165.74	440.78
120	0.1495	6,340,889	271.32	331.5	440.78
130	0.0254	6,977,740	271.32	10.366	440.78
B84 Model					
Storage pressure [bar]	Orifice diameter [m]	Equivalent Diameter [m]	Static Temperature T_3 [K]	Mass flowrate [kg/s]	Speed of sound v_3 [m/s]
2.5	0.0254	0.0285	300	0.1993	440.78
32.5	0.0254	0.1031	300	2.5915	440.78
65	0.0127	0.0729	300	1.2957	440.78
65	0.0381	0.2187	300	11.662	440.78
65	0.0508	0.2916	300	20.732	440.78
65	0.1016	0.5833	300	82.93	440.78
65	0.2540	1.4582	300	518.32	440.78
100	0.0254	0.1808	300	7.974	440.78
130	0.0254	0.2062	300	10.366	440.78
B87 Model					
Storage pressure [bar]	Orifice diameter [m]	Equivalent Diameter [m]	Static Temperature T_3 [K]	Mass flowrate [kg/s]	Speed at level 3 v_3 [m/s]
2.5	0.0254	0.0283	278.15	0.1993	416.32
32.5	0.0254	0.0814	278.15	2.5915	654.06
65	0.0127	0.0571	278.15	1.2957	663.96
65	0.0381	0.1715	278.15	11.662	663.96
65	0.0508	0.2287	278.15	20.732	663.96
65	0.1016	0.4575	278.15	82.93	663.96
65	0.2540	1.1438	278.15	518.32	663.96
100	0.0254	0.1415	278.15	7.974	667.43
130	0.0254	0.1611	278.15	10.366	668.91

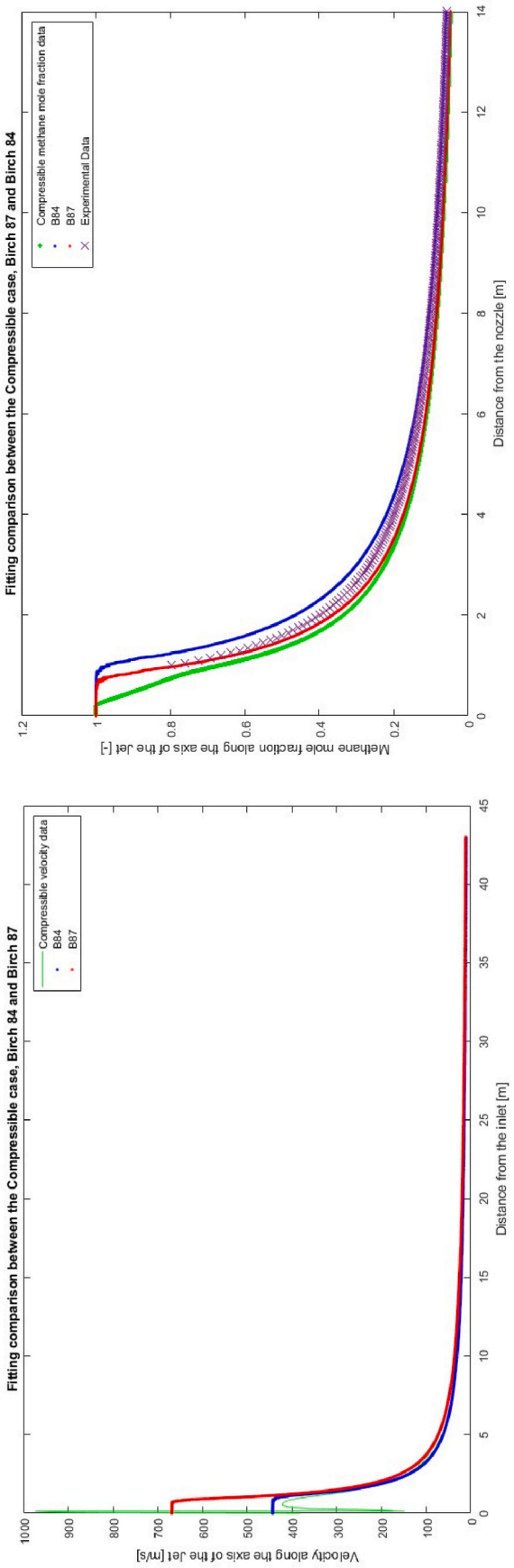

Fig. 4. Comparison between the velocity profile along the jet-axis of each model of the base case (left) and mole fraction of the jet with experimental data from Birch et al. (1984) (right).

All simulations were performed as a stationary model, with the Coupled solver and the second upwind scheme. As a convergence criterion, the default Fluent settings were used which hinges on residual values to be reduced under orders of magnitude of 10^{-3} for all parameters except for energy, which has an order of magnitude of 10^{-6}.

2.4. Criteria of analysis

The simulation methodology explored in the previous sections was the basis for all subsequent cases studied in the present work. The analysis was extended to varying release conditions, along with a set of cases with different real orifice diameter. Cases are listed in Table 5, and by including base scenario cases, there is a total of 32 cases.

The compressible model is seen as the more reliable model between the 3 being tested, as it is able to satisfactorily model experimental data of underdeveloped jets from Birch et al. [16], which was demonstrated by Novembre et al. [28]. The compressible case was treated as the *de facto* experimental data, which the incompressible models were compared to.

2.4.1. Position of the equivalent diameter and data management

To avoid any boundary effect, that is a numerical instability on the inlet once the nozzle velocity is two orders of magnitude higher than the wind velocity, the methane inlet was positioned at $\frac{Lenght\ [m]}{D_{eq}} = 50$, which is roughly 7 m from the cardinal origin along the z-axis (this was chosen equal for all the simulation to have the same origin for all of them). Fig. 4 displays a clear comparison of all three models by aligning their data points, revealing the distinct differences among each. The velocity profile along the axis of the jet undergoes significant changes within the nearfield zone, while the mole fraction is compared to experimental data from Birch et al. [16], with satisfactory agreement across all models. Fig. 5 presents a comparison based on the velocity contours.

This outcome is achieved by assuming that the positioning of the real orifice and the notional diameter of the simplified models coincide, which addresses the question of the virtual source's position in the domain relative to the actual leak. This assumption is further supported by the velocity profile of each model, where the potential core of the incompressible jet extends to almost the same length as the nearfield zone of the compressible jet. Therefore, no distance between the real source and the virtual source is required to accurately simulate a high-pressure jet when utilizing the incompressible model approach.

The potential core of both incompressible jets models is prevented from mixing with the ambient fluid due to the presence of a shear layer between the potential core and its surroundings. The shear layer is created as a consequence of significant velocity gradient between the core and the environment [31]. Subsequently, the potential core of the incompressible jet remains at a stable velocity as friction with the surrounding environment is diminished. On the other hand, the compressible jet, due to its expansion and recompression, displays an undulating pattern in its velocity profile [5].

Trying to define the goodness of fit between the three models can become complicated if the nearfield zone is considered. The aim of the simplified models is to properly simulate the farfield without having to simulate the nearfield, as such, the data to be compared must be carefully selected.

In the vein of avoiding any bias, the discriminating parameter of where to splice the data for each model was chosen from the compressible model. Two splits were performed on the data taken from the axisymmetric axis of the jets with the following criteria:

- To avoid unfairly judging the goodness of the incompressible model by including the nearfield zone, a data splice for all models was performed at the distance where the pressure is 0.1% above operating pressure in the compressible model (101,500 Pa), considering that this is the point in which the transition zone ends. From this

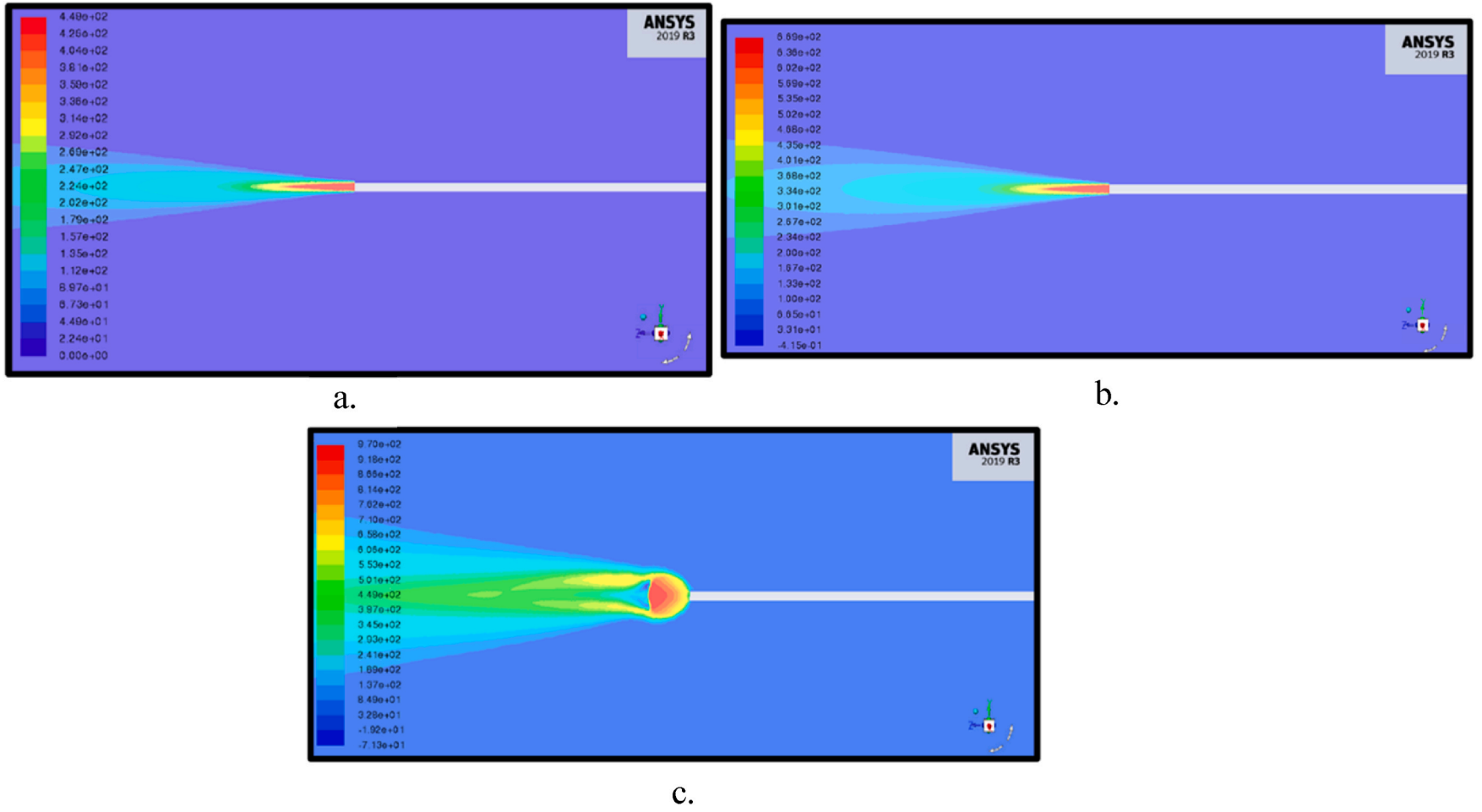

Fig. 5. Comparison between the velocity contour of the B84 model (a), B87 model (b) and the compressible model (c) at 65 bar of storage pressure and a 0.5 inch real orifice. In figure (a) and (b) the potential core has a velocity peak of 449 m/s and 669 m/s respectively at the notional orifice, as opposed to figure (c), where the Mach disk in the nearfield zone can be clearly seen with a velocity peak of 970 m/s.

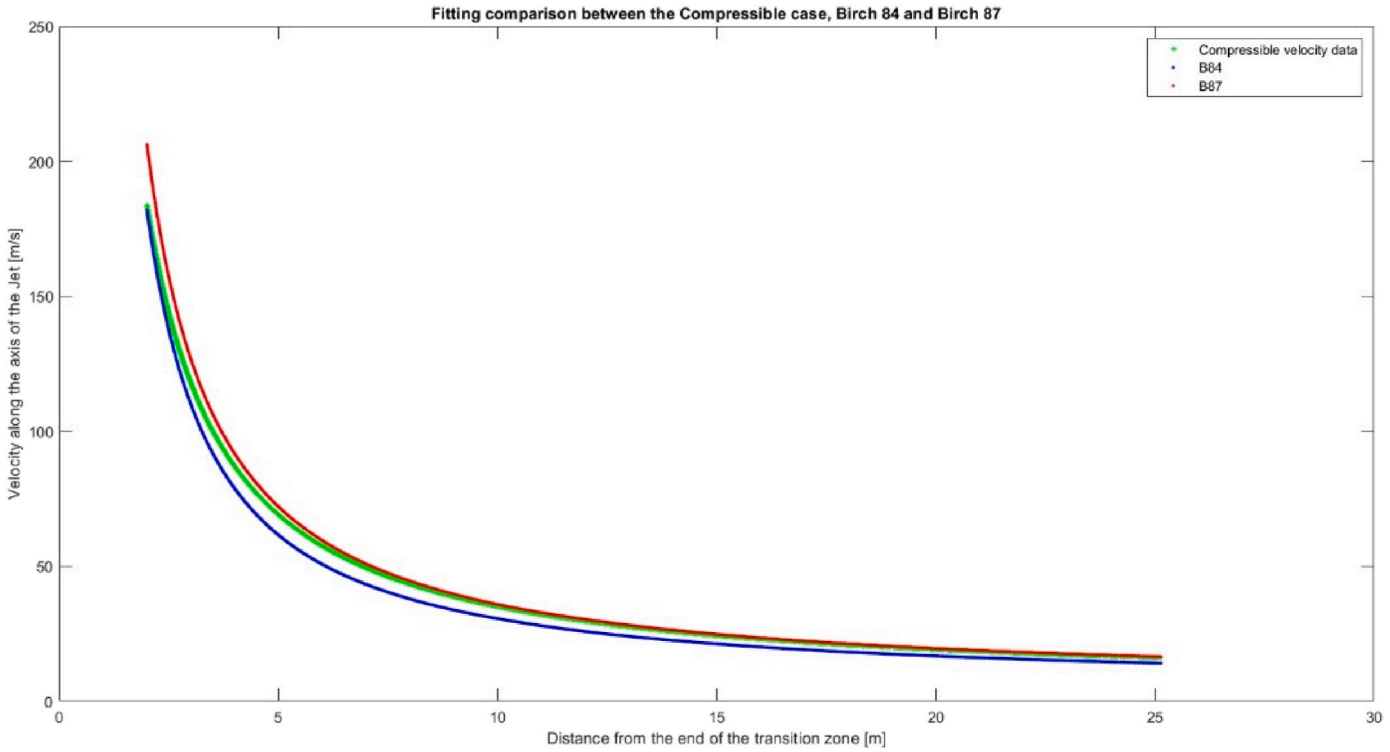

Fig. 6. Data comparison between each model for the velocity profile along the jet axis of the case shown in Fig. 3 (left). The same number of data points were used to compare each model, where the splices were performed at 1.99 m and 25.14 m.

point on, the axial pressure of the jet decrease asymptotically towards operating pressure with no further fluctuations [5].

- To make sure that the same number of points close to the nearfield are used for the statistical analysis for each model (see 3.2.2), a second data splice was performed at the distance where the pressure is equals to the operating pressure (101,325 Pa) in the compressible model.

As a way of example, illustrated in Fig. 6, the velocity profile data set was spliced along the jet axis of the base case for all considered models. By comparing Figs. 4 and 6, it is clear that all effects related to pressure fluctuations were excluded, only leaving the farfield zone as raw data. Thus, the same amount of data points is used for each model to properly measure the variance of the incompressible models to the compressible model.

2.4.2. Model evaluation statistics

The fitting goodness of each case judged based on the statistical analysis method introduced by Hanna [32], which plots in a logarithmic graph the Geometric Variance (GV) and Geometric Mean Bias (GM) with the following equations:

$$GV = \exp\left[\overline{ln\left(\frac{Y_i}{\widehat{Y}_i}\right)}\right]^2 \tag{16}$$

$$GM = \exp\left[\overline{ln\left(\frac{Y_i}{\widehat{Y}_i}\right)}\right] \tag{17}$$

The $\widehat{Y}_i$ is the value predicted by the model at a given distance, Y_i is the experimental value at the same distance, while $\overline{Y}$ is the mean value of the experimental data set. Furthermore, if no random scatter is present, all values will have a minimal amount of GV, given a GM value. This parabola behaviour is described by the following equation:

$$\ln(GV) = (\ln(GM))^2 \tag{18}$$

According to Chang and Hanna [33], a "good" model should have a relative GM that is less than 30%, meaning a value of $0.7 < GM < 1.3$.

3. Results and discussion

In the following sections results from the simulated cases are discussed. Mach disk and the structure of a compressible jet with multiple release conditions is studied to assess the capability of the model to simulate the most dynamically complicated sections of the jet. Subsequentially, the aim was unearthing the inherent ability of these simplification models to replicate the molar fraction, temperature, and velocity profile of the compressible jet along its axis. Data obtained from the post-processing step from the Ansys® software were compiled and compared using MATLAB to quantify, through appropriate statistical values, their reliability.

3.1. Mach disk location estimated by the compressible model

The cases that were considered had a combination of real orifice diameter and pressure variation. While the velocity of release for the compressible model is fixed to the speed of sound, most of the changes between one case to the other will be due to a shift in density and surface inlet area. Since there is no readily available data for high pressure jets with very large diameters [28], a "local" check was performed for the development of the nearfield zone with the study of the Mach disk.

The Mach disk is a heavily studied phenomenon that manifest itself as a normal shock wave, as intercepting shock waves (defined as oblique shock waves due to a Prandtl-Meyer expansion of an extremely underdeveloped jet) coalesce into a singular intercepting point. The positioning of the Mach disk indicates the location of reduced compressible effects, as pressures are very close to atmospheric after the expansion and recompression of the jet [5].

The following formula can be used to estimate the positioning of the Mach disk [5]:

Table 6
Comparison between simulated and calculated (Eq. (19)) Mach disk distance.

Storage pressure [bar]	Orifice diameter [m]	Calculated X_{mach} [m]	Simulated X_{mach} [m]
2.5*	0.0254	–	–
32.5	0.0254	0.0928	0.0926
65	0.0127	0.0656	0.0656
65	0.0254	0.1312	0.1292
65	0.0381	0.1968	0.205
65	0.0508	0.2624	0.2621
65	0.1016	0.5248	0.5247
100	0.0254	0.1627	0.1601
100	0.1158	0.7365	0.7368
120	0.1495	1.0528	1.0525
130	0.0254	0.1855	0.1854

* For this value it is not possible to compute a Mach disk value, since the ratio of storage pressure and atmospheric pressure is below the necessary critical value ($\eta = \frac{P_1}{P_3} \geq 7$) for the collapse of intercepting shock waves into a normal shock wave, instead developing as a series of shock diamonds.

$$X_{mach} = 0.645\sqrt{\frac{P_1}{P_3}}d \tag{19}$$

Validation of the compressible model was done by comparing the Mach disk positioning estimated by equation (16) and the one simulated. Results are shown in Table 6:

3.2. End of the transition zone at varying pressures and orifice diameters

The transition zone is defined as the point at which there is a homogenization of the pressure field [5], with small variable variation both longitudinally and radially. This point is not explicitly defined in current literature. To adhere to the previous definition, this point was defined by indicating the distance from the nozzle at which the absolute pressure reaches a value above 0.1% of the operating pressure along the symmetrical axis of the jet within the compressible model. From this distance on, the pressure along the axis decreases asymptotically towards operating pressure. Like the distance from the inlet nozzle to the Mach disk, the distance to the ending of the transition zone is also dependant on the pressure ratio between the storage conditions and cut-off conditions, and the orifice diameter. This distance can be described by the following equation, as illustrated in Fig. 7:

$$X_{ETZ} = 2.729\sqrt{\frac{P_1}{P_3}}d^{0.68} \tag{20}$$

Fig. 7 shows that the correlation works especially well for cases where the diameter of the orifice is below 4.6 inches (0.1158 m). Within the wide range of pressures studied, from 2.5 to 130 bar, the analytical correlation can be used for the estimation of the end of the transition zone.

3.3. Goodness of fit of incompressible models – varying storage pressure at 1-inch real orifice diameter

Regardless of the model utilized, determining the critical pressure (P_2) at the orifice is solely reliant on the storage pressure. The compressible model employs the flow rate calculated using the actual orifice diameter and critical pressure, while the incompressible models use the diameters calculated with equations (10) and (14) for B84 and B87 at atmospheric pressure, respectively. Due to the higher velocities predicted by B87, the equivalent diameter predicted is consistently smaller than B84, and their differences increase with storage pressure, as demonstrated in Table 5. Fig. 8 illustrates how pressure directly impacts the ability of the incompressible models to replicate the molar fraction, temperature, and velocity profiles predicted by the compressible model.

It was found that both models are capable of replicating the data predicted by the compressible approach, with some caveats that must be recognised. While at low pressures the equivalent diameters models are basically indistinguishable, as the storage pressure increases, so does their fallibility. It is evident that the approach used to estimate the inlet velocity of each model is the defining factor for diverging results. B84 assumes that the initial velocity will always be the speed of sound of

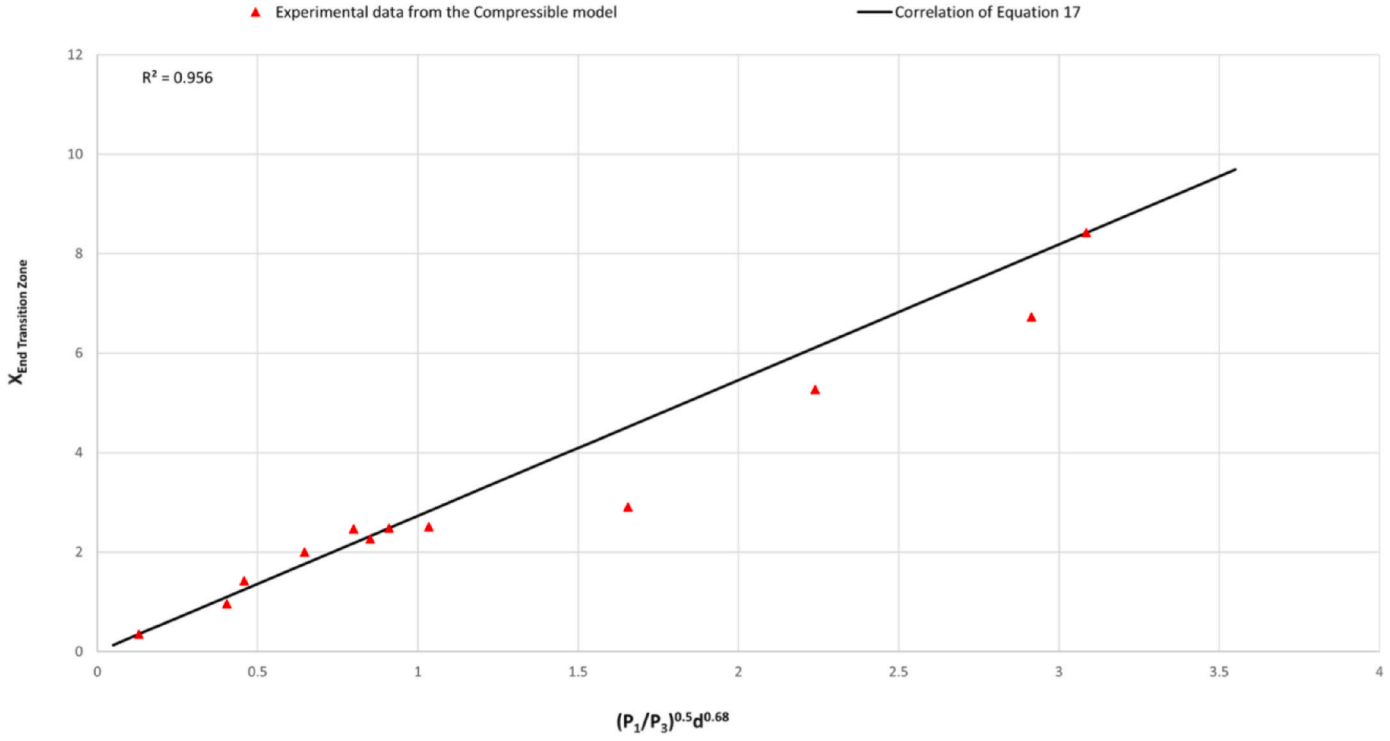

Fig. 7. Spatial position of the end of the transition zone along the jet axis, estimated from the compressible model. Correlation uses Eq. (20).

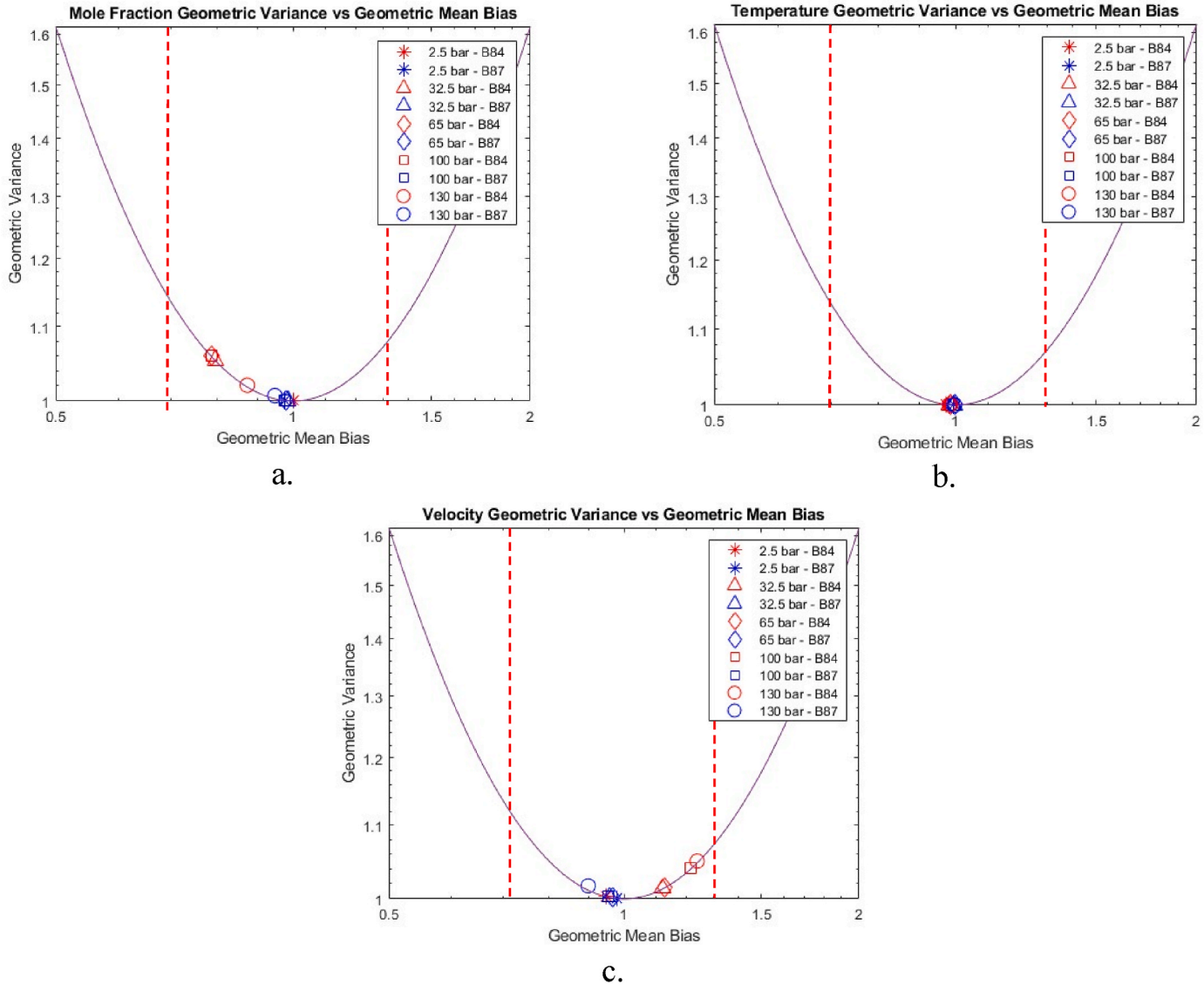

Fig. 8. Geometric Mean Bias (GM) against Geometric Variance (GV) between predictions made of the near field zone by the incompressible models, B84 (Red) and B87 (Blue) and the compressible model at varying storage pressure with a constant real orifice diameter of 1 inch. Each graph describes the goodness of fit of each incompressible model with the compressible model for the mole fraction (a), temperature (b) and velocity (c) profiles. (For interpretation of the references to colour in this figure legend, the reader is referred to the Web version of this article.)

methane at 300 K, which comes to 440.78 m/s. Although it is a reasonable assumption where the compressible model and B84 have the same inlet velocity, the expansion and recompression of the jet in the compressible model alters the development of the velocity profile. B87 attempts to account for this effect by overpredicting the inlet velocity to values close to 660 m/s with a smaller area of the virtual source. This is a consequence of the momentum conservation assumption made by the latest model, which tries to make up for one of the biggest flaws of the incompressible model approach: the potential core is completely unaffected by air entrainment during the expansion of the jet. This can be clearly seen on Fig. 4, where the velocity and mole fraction of B84 and B87 remain at a constant value for several centimetres away from their source.

Such a simplification does come with the cost of loss accuracy as the simulated case becomes more extreme. While still showcasing acceptable results when comparing with the compressible model, at 130 bar, both incompressible model approaches falter. This behaviour is intrinsic to the hypothesis of incompressibility made by B84 and B87, where, at such a massive jump in pressure, it is harder to justify. Simulation instabilities and solver fine-tuning (*i.e.,* applying more appropriate relaxation factors) were necessary to satisfy the convergence criteria for mole fraction residuals.

It is evident from the onset that B87 is more adept at predicting the temperature profile at the centreline of the jet than B84. B87 starts by assuming an initial temperature equals to its storage, while B84 has a fixed value for bulk temperature. Nevertheless, from the study of the GM, the overprediction of the temperature profile does not deviate much from the compressible model profile. Since B84 predicts a constant value of 300 K for the temperature along the axis of the jet, the overprediction, in the worst of cases, is less than 7%. The lowest values predicted by the compressible model is 282.48 K in the 2.5 bar case, at the distance of the first splice. Furthermore, the velocity with which air is englobed by the jet within the compressible model leads to a fast increase in temperature in the first 3 m from the source, reaching ambient temperature. This then allows to have reasonable results from both incompressible models for sections of the jet away from the nearfield zone.

Despite the varying in quality of simulations between models, both incompressible models fall within the definition of a “good model”

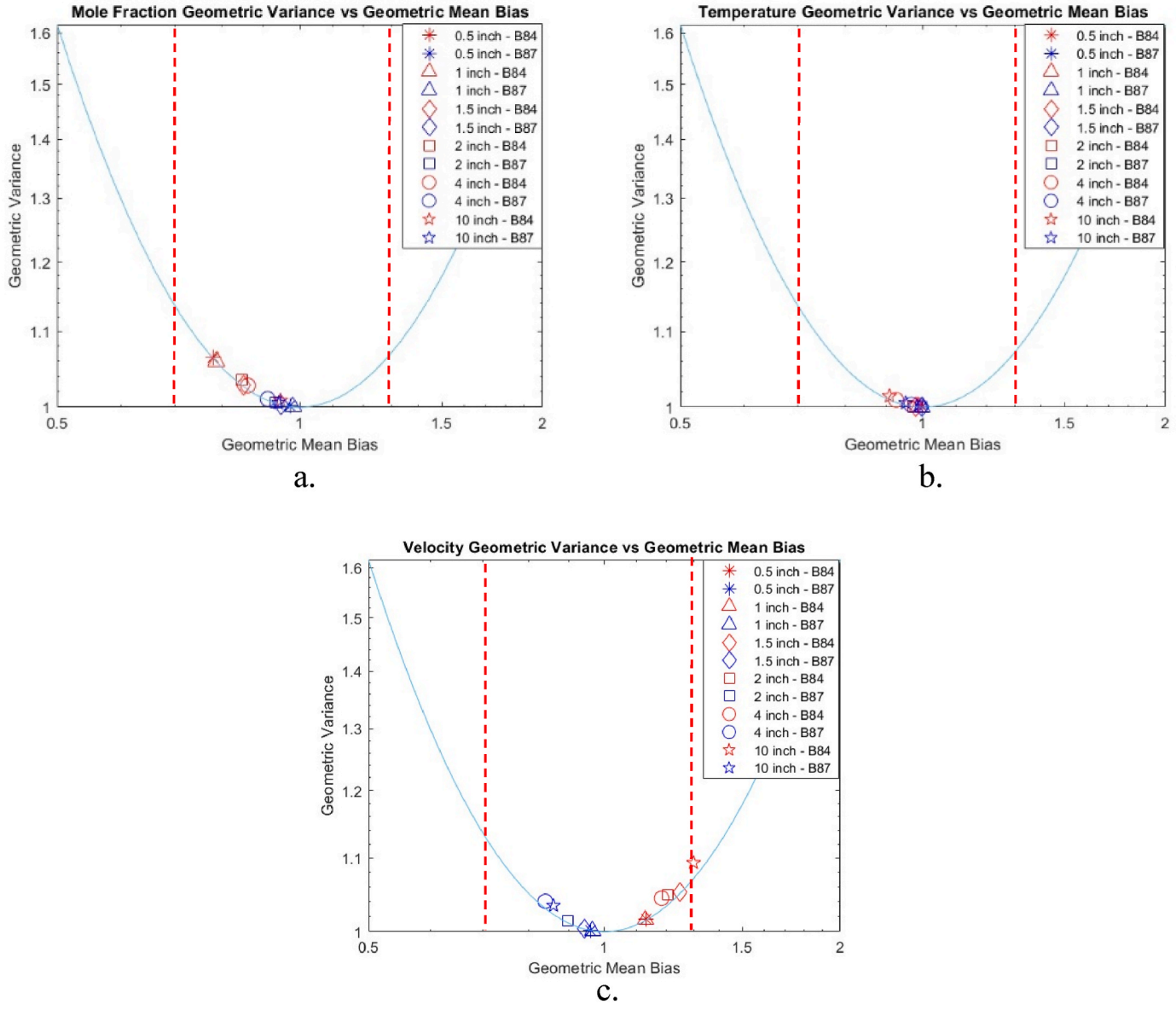

Fig. 9. Geometric Mean Bias (GM) against Geometric Variance (GV) between predictions made of the near field zone by the incompressible models, B84 (Red) and B87 (Blue) and the compressible model at varying real orifice diameter at a constant storage pressure of 65 bar. Each graph describes the goodness of fit of each incompressible model with the compressible model for the mole fraction (a), temperature (b) and velocity (c) profiles. (For interpretation of the references to colour in this figure legend, the reader is referred to the Web version of this article.)

described in section 2.4.2. B87 is the superior model for all scenarios up to pressures of 130 bar and 1-inch orifice diameter, as it better models how the temperature and velocity profile develops along its axis beyond the transition zone.

3.4. Goodness of fit of incompressible models – varying real orifice diameter at 65 bar storage pressure

Critical pressure at the orifice will always be the same for a given pressure, independent of orifice size. By using the storage temperature of 278.15 K, the temperature drop will always be the same and the initial speed will remain the speed of sound at the real orifice. The change in the real orifice will not influence the thermodynamic state of the system but will instead change the flow rate through the real orifice.

As shown in Fig. 9, the orifice diameter has a direct effect on the capacity of incompressible models to replicate results from the compressible model. The critical pressure with which jets on this section are released will always be the same, although it does not mean that the nearfield zone will also be identical. Due to the larger orifice for each simulation, the positioning of the Mach disk will also vary, increasing in horizontal distance from the real orifice, as shown in Table 6. This will have a direct effect on the ability of each incompressible model to properly portray the various profiles after the potential core.

While Figs. 8 and 9 have similar results, a more scattered pattern from Fig. 9 can be identified. Though results from B87 are more in par with the compressible model than B84, these are less consistent as the orifice size increases. The underprediction of the velocity dissipation of B87 leads to an overprediction of the mole fraction, although not as deep as B84. This change from the previous section is related to the mass flow rate that each model is able to handle. When increasing the storage pressure, the mass flow rate increment is linear, meanwhile, when increasing the diameter size, the increment is quadratic. With a larger diameter, the potential core of the incompressible models, which is already affected by the assumption of no air entrainment, is further protected from the surrounding environment by a larger shear layer. Thus, the use of incompressible models to predict ever-increasing flow

rates becomes more conservative, until it fails, as shown in Fig. 9c by B84 at a 10-inch diameter. Like in the previous section, some effort was needed to meet the conversion criteria of the models, as the high flow-rate and rapid velocity dissipation can tax the solver.

Similar observations from the previous sections can be made for the ability of each model to predict the temperature profile. Nevertheless, as the size of the orifice gets pushed to extreme sizes, hypothesis like the ones made by B84 start showing cracks, with the lowest value is reached for the largest diameter at 10 inches, with 233.51 K at the first splice, an overprediction of 28.47%.

Through this analysis it was evidenced that the change in orifice diameter has a larger effect in the ability of incompressible models to perform, when compared to pressure variation cases. B87 always falls within the "good model" limit imposed in section 2.4.2, which makes it the go-to model to use to simulate a high-pressure jet release, when the use of a compressible model is not possible. On the other hand, while B84 is still very much capable of giving satisfactory results, using it is very much dependant on the type of analysis that is being performed, either related to mole fraction dissipation, where results are still acceptable for all orifice sizes, or velocity dissipation, where it has a hard limit at 25 cm (10 inches).

4. Conclusions

In this paper, three CFD approaches for high pressure natural gas jets were compared. The compressible model approach simulates the jet in its entirety, leading to more accurate results, but computationally expensive calculations. The incompressible model approaches, namely B84 and B87, sidestep the simulation of the nearfield zone, the most dynamically complicated section of the jet, with the assumption of non-compressibility.

A wide range of cases were simulated to verify the validity and applicability of the incompressible models instead of the compressible one. The findings of this paper can be summed up as follows:

- It was demonstrated in section 2.4.1 that the length of the potential core of the incompressible model and the nearfield zone of the compressible model are of the same size, implying that the position of the real source and the virtual source must coincide.
- An empirical correlation for the position of the end of the transition zone (*i.e.,* the beginning of the farfield zone) was possible to relate in section 3.2. This is dependant in the pressure dissipation rate along the axis of the jet after the expansion.
- The no-compressibility assumption has a strong effect on the reliability of the incompressible models, where they bring some turbulent instabilities in the simulation at pressures of 130 bar and orifice diameters of 4 and 10 inches.
- When the temperature of the jet is an essential part of the studied case, like the heat transfer between a jet and an impinged object, B87 must be used due to the unreliability of B84.
- Both incompressible models can be a good alternative to the compressible model, up and until cases that simulate "full bore" (10 inches diameter size) releases, where B84 becomes unreliable.

Many more release modes can be explored, further expanding the understanding on how limited the incompressible model is as a tool. Moreover, the empirical correlation in section 3.2 is dependent on the estimation of the internal pressure dissipation rate of the jet and must be verified through experimental tests.

CRediT authorship contribution statement

Fabio Ferrario: Formal analysis, Software, Writing – original draft, Investigation, Methodology. **Valentina Busini:** Conceptualization, Data curation, Methodology, Project administration, Supervision, Writing – review & editing.

Declaration of competing interest

The authors declare that they have no known competing financial interests or personal relationships that could have appeared to influence the work reported in this paper.

Data availability

Data will be made available on request.

Acknowledgements

This work was realised with the collaboration of the European Commission Joint Research Centre under the Collaborative Doctoral Partnership Agreement No. 35455.

References

[1] Y. Deng, H. Hu, B. Yu, D. Sun, L. Hou, Y. Liang, A method for simulating the release of natural gas from the rupture of high-pressure pipelines in any terrain, J. Hazard Mater. 342 (2018) 418–428, https://doi.org/10.1016/j.jhazmat.2017.08.053.
[2] D.A. Crowl, J.F. Louvar, Chemical Process Safety: Fundamentals with Applications, second, 2002.
[3] P. Bénard, A. Hourri, B. Angers, A. Tchouvelev, Adjacent surface effect on the flammable cloud of hydrogen and methane jets: numerical investigation and engineering correlations, Int. J. Hydrogen Energy 41 (41) (2016) 18654–18662, https://doi.org/10.1016/j.ijhydene.2016.08.173.
[4] MATHESON TRI-GAS, INC., 'Methane - Safety Data Sheet', Safety Data Sheet, 2009.
[5] E. Franquet, V. Perrier, S. Gibout, P. Bruel, Free underexpanded jets in a quiescent medium: a review, Prog. Aero. Sci. 77 (2015) 25–53, https://doi.org/10.1016/j.paerosci.2015.06.006.
[6] A. Fiorucci, et al., Risk assessment of dangerous products release and dispersion: a comparison between CFD and integral models, in: CISAP3, 13, 2008.
[7] H.K. Versteeg, W. Malalasekera. An Introduction to Computational Fluid Dynamics - the Finite Volume Method, Second, Pearson, 2007.
[8] Md J. Hasan, K. Tawkir, A.A. Bhuiyan, Improvement of an exhaust gas recirculation cooler using discrete ribbed and perforated louvered strip vortex generator, Int. J. Thermofluids 13 (2022) 100132, https://doi.org/10.1016/j.ijft.2022.100132.
[9] F. Hossain, M.J. Hasan, M.Z. Sarkar, M.R. Karim, A.A. Bhuiyan, Prediction of carbon capture and sequestration (CCS) technology in a 125 MW tangentially coal-fired subcritical thermal power plant for retrofitting in Bangladesh, Results Eng. 18 (2023) 101159, https://doi.org/10.1016/j.rineng.2023.101159.
[10] C.J. Greenshields, OpenFOAM - the Open Source CFD Toolbox, 3.0.1, OpenFOAM Foundation Ltd., 2015 [Online]. Available: https://foam.sourceforge.net/docs/Guides-a4/ProgrammersGuide.pdf.
[11] Ansys inc, ANSYS Fluent Theory Guide, 2013 vol. Release 15.
[12] A. Reyes-Urrutia, C. Venier, N.J. Mariani, N. Nigro, R. Rodriguez, G. Mazza, A CFD comparative study of bubbling fluidized bed behavior with thermal effects using the open-source platforms MFiX and OpenFOAM, Fluid 7 (1) (2021) 1, https://doi.org/10.3390/fluids7010001.
[13] C. Colombini, A. Martani, R. Rota, V. Busini, Ground influence on high-pressure methane jets: practical tools for risk assessment, J. Loss Prev. Process. Ind. 67 (2020) 39–59, https://doi.org/10.1016/j.jlp.2020.104240.
[14] C. Colombini, C. Iannantuoni, R. Rota, V. Busini, Unignited high-pressure methane jet impacting a cylindrical obstacle: an assessment tool for consequences analysis, J. Loss Prev. Process. Ind. 76 (2022) 104593, https://doi.org/10.1016/j.jlp.2021.104593.
[15] C. Colombini, E. Carminati, A. Parisi, R. Rota, V. Busini, Safety evaluations on unignited high-pressure methane jets impacting a spherical obstacle, J. Loss Prev. Process. Ind. 74 (2022) 104631, https://doi.org/10.1016/j.jlp.2021.104631.
[16] A.D. Birch, D.R. Brown, M.G. Dodson, F. Swaffield, The structure and concentration decay of high pressure jets of natural gas, Combust. Sci. Technol. 36 (5–6) (1984) 249–261, https://doi.org/10.1080/00102208408923739.
[17] B.C.R. Ewan, K. Moodie, Structure and velocity measurements in underexpanded jets, Combust. Sci. Technol. 45 (5–6) (1985) 275–288, https://doi.org/10.1080/00102208608923857.
[18] A.D. Birch, D.J. Hughes, F. Swaffield, Velocity decay of high pressure jets, Combust. Sci. Technol. 52 (1–3) (1987) 161–171, https://doi.org/10.1080/00102208708952575.
[19] R.W. Schefer, W.G. Houff, T.C. Williams, B. Bourne, J. Coulton, Characterization of high-pressure, underexpanded hydrogen-jet flames, Int. J. Hydrogen Energy 32 (2007) 2081–2093, https://doi.org/10.1016/j.ijhydene.2006.08.037.
[20] W. Cui, Y. Yuan, L. Tong, B. Shen, Numerical simulation of hydrogen leakage diffusion in seaport hydrogen refueling station, Int. J. Hydrogen Energy 48 (63) (2023) 24521–24535, https://doi.org/10.1016/j.ijhydene.2023.03.208.
[21] C. Colombini, V. Busini, Obstacle influence on high-pressure jets based on computational fluid dynamics simulations, Chem. Eng. Trans. 77 (2019) 811–816, https://doi.org/10.3303/CET1977136.

[22] C. Colombini, M. Pontiggia, G. Uguccioni, R. Rota, V. Busini, Ground influence on high-pressure methane jets: different concentration clouds scenarios, Chem. Eng. Trans. 86 (2021) 541–546, https://doi.org/10.3303/CET2186091.
[23] E. Papanikolaou, D. Baraldi, Comparison of Modelling Approaches for CFD Simulations of High Pressure Hydrogen Releases, Joint Research Centre, JRC, 2011. http://conference.ing.unipi.it/ichs2011/papers/168.pdf.
[24] F.R. Menter, Two-equation eddy-viscosity turbulence models for engineering applications, AIAA J. 32 (8) (1994) 1598–1605, https://doi.org/10.2514/3.12149.
[25] M. Forsell, Numerical Modelling of Accidental Gas Release in a Gas Turbine Enclosure- Evaluation of Notional Nozzle Models and Dispersion Modelling Using RANS, URANS and LES Methods, Chalmers University of Technology, 2019 [Online]. Available: https://odr.chalmers.se/items/408cff37-d8a9-4665-b853-86c45aeb04ac.
[26] X. Li, J. Bi, D. M. Christopher, 'Comparison of Numerical and Algebraic Models of Low and High Pressure Hydrogen Jet Flows With Ideal And Real Gas Models', 2013 [Online]. Available: http://www.ichs2013.com/images/papers/186.pdf.
[27] R.H. Perry, D.W. Green. Perry's Chemical Engineering Handbook, eighth ed, McGraw-Hill Professional, 2007.
[28] N. Novembre, F. Podenzani, E. Colombo, Numerical study for accidental gas releases from high pressure pipelines, Eur. Conf. Comput. Fluid Dyn. (2006) [Online]. Available: https://repository.tudelft.nl/islandora/object/uuid:1e51218d-fa17-42dd-afad-14f4092202e7.
[29] G. Romano, P. Tombini, F. Ferrario, A. Mormile, V. Busini, High-pressure jet and cylindrical obstacles in series: a CFD study, in: Eur. Saf. Reliab. Conf. ESREL 2022, vol. 32, 2022, pp. 150–157, https://doi.org/10.3850/978-981-18-5183-4_R04-03-475-cd.
[30] G. Romano, P. Tombini, P. Blas, V. Busini, 'Multi-obstacles influence on high-pressure methane jets', 31st Eur. Saf. Reliab. Conf., vol. 31, 2021, pp. 638–643, doi: 10.3850/978-981-18-2016-8_348-cd.
[31] H.B. Awbi, Ventilation of Buildings, second ed., Routledge, 2003.
[32] S.R. Hanna, J.C. Chang, D.G. Strimaitis, Hazardous gas model evaluation with field observations, Atmos. Environ. 27A (15) (1993) 2265–2285, https://doi.org/10.1016/0960-1686(93)90397-H.
[33] J.C. Chang, S.R. Hanna, Air quality model performance evaluation, Meteorol. Atmos. Phys. 87 (1–3) (2004), https://doi.org/10.1007/s00703-003-0070-7.